Experimental investigation of hypersonic boundary layer transition delay by means of ultrasonically absorptive carbon-carbon material in the High Enthalpy Shock Tunnel Göttingen (HEG)

Alexander Wagner, Markus Kuhn,
Viola Wartemann, Jan Martinez Schramm, Klaus Hannemann
German Aerospace Center (DLR)

May 30th, 2013

Contents

1 Introduction

Laminar to turbulent transition in high-speed boundary-layers leads to a significant increase of wall shear stress and wall heat flux. Thus, the performance and the thermal protection system of hypersonic vehicles are strongly affected. The increase of the laminar portion of the boundary layer is of critical importance to the design and optimization of these vehicles, Force (1992). This motivates the development of hypersonic laminar flow control concepts.

For small free-stream disturbances and negligible surface roughness the second-mode instability is the dominant instability in predominantly two-dimensional boundary layers at hypersonic speeds, Malik (1989). Wall temperatures below the recovery temperature as present e.g. on hypersonic vehicles are known to stabilize the first mode and to destabilize the second-mode instability. Both facts serve as basis for the concept developed by Fedorov et al. (2001) and Malmuth et al. (1998) to passively control transition on hypersonic vehicles using ultrasonically absorptive surfaces. The hypothesis that such materials can massively reduce the amplification rate of the second-mode by absorbing the disturbance energy and thus to delay the transition onset was shown theoretically by Fedorov et al. (2001) using linear stability theory. Rasheed et al. (2002) experimentally confirmed the stabilizing effect by showing a delay of the transition onset using a porous surface with regularly spaced cylindrical blind holes on a sharp 5° half-angle cone at Mach 5 in the T-5 high-enthalpy shock tunnel of the California Institute of Technology. It was demonstrated that if the pore size is significantly smaller than the viscous length scale a porous surface is highly effective in delaying second-mode dominated boundary-layer transition. Further studies on ultrasonically absorptive surfaces with regular microstructure were conducted by Fedorov et al. (2006) in the ITAM T-326 Mach 6 hypersonic wind tunnel on a 7° half-angle sharp cone. Hot-wire measurements conducted in the scope of these studies revealed that the porous surface weakly amplifies the first mode, due to the surface roughness, but stabilizes the second-mode which was identified to be the dominant instability.
Analogous measurements using a thin coating of fibrous absorbent material (felt metal) with random microstructure were carried out by Fedorov et al. (2003). The material is of particular interest since its random microstructure is typical for practical TPS (thermal protection system) materials. Hot-wire measurements in the laminar boundary-layer revealed a reduction of the second-mode instability and thus the potential to delay transition onset. Maslov et al. (2006) and Maslov et al. (2008) confirmed the assumption by showing a significant increase of laminar run on a sharp 7° half-angle cone which was equipped with felt metal and tested in the AT-303 ITAM wind tunnel at Mach 12 and in the ITAM impulse hypersonic wind tunnel Transit-M at Mach 6.

The cavity depth and the surface porosity were numerically identified as the parameters dominating the effectiveness of the porous surface, Brès et al. (2010); Wartemann et al. (2012a). In particular the impact of the pore depth was investigated experimentally by Lukashevich et al. (2012). A pore depth about 50 % higher compared to the effective pore diameter was found as an optimum. The optimal porous layer thickness leads to a phase cancellation and thus to maximum stabilization of the second-mode waves. A

further increase of the pore depth leads to a decrease of the stabilization and finally tends towards the deep pore limit, Wartemann et al. (2012b).

Based on the promising results obtained on porous surfaces with regular and random microstructures and based on the fact that the majority of the TPS materials have random microstructures, a material with practical TPS potential was used for the first time for passive transition control. The chosen carbon fibre reinforced carbon (C/C) offers high temperature stability in absence of oxygen. It represents an intermediate state of C/C-SiC which has been used successfully as TPS on hypersonic vehicles, Turner et al. (2006); Weihs et al. (2008). Previous experimental studies on 7° half-angle blunted cones in the DLR High Enthalpy Shock Tunnel Göttingen (HEG) at Mach 7.4 confirmed that the transition process is dominated by the second-mode instability, Wagner et al. (2011); Laurence et al. (2012); Wagner et al. (2012). The HEG conditions used in these studies served as baseline test environment for the present investigations.

The present article focuses on the design and the manufacturing of the wind tunnel model and in particular on the manufacturing and characterization of the carbon-carbon material. Boundary layer disturbances on the model were measured by means of surface pressure fluctuations for a range of unit Reynolds numbers. A stabilization of the second-mode instability and an increase of the laminar portion of the boundary layer on the porous surface was observed.

2 High Enthalpy Shock Tunnel Göttingen (HEG)

The HEG was commissioned for use in 1991. Since then it has been used extensively in a large number of national and international space and hypersonic flight projects. Originally, the facility was designed for the investigation of the influence of

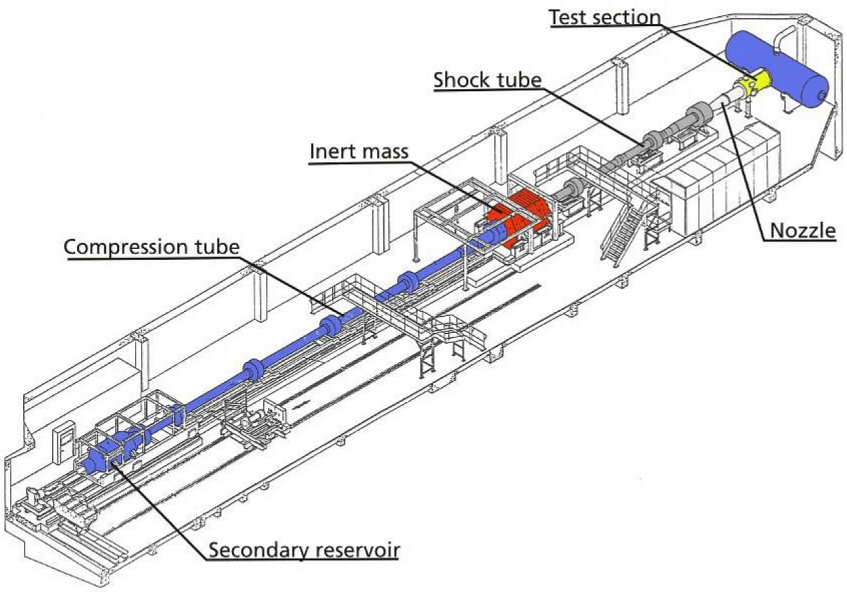

Figure 1: Schematic of HEG.

high temperature effects such as chemical and thermal relaxation on the aerothermodynamics of entry or re-entry space vehicles. In this operating range, total specific enthalpies of up to 23 MJ/kg and nozzle stagnation pressures of up to 150 MPa can be reached. In recent years its range of operating conditions has been subsequently extended, the main emphasis being to generate new test conditions which allow investigating the flow past hypersonic flight configurations from low altitude Mach 6 up to Mach 10 at approximately 33 km altitude, Hannemann and Martinez Schramm (2007); Hannemann et al. (2008).
An overview of the HEG shock tunnel is provided by the schematic in **figure 1**. The overall length and mass of the facility are 60 m and 280 t, respectively. The shock tunnel consists of a secondary reservoir, a compression tube, separated from an adjoining shock tube by the primary diaphragm, and a subsequent nozzle and test section. For a test in HEG pressurized air in the secondary reservoir is used to accelerate the piston down the compression tube. The driver gas in the compression tube is compressed quasi-adiabatically and leads to the main diaphragm rupture when the burst pressure is reached. Subsequently, a strong shock wave propagates down the shock tube being reflected at the end wall. The reflected shock provides the high pressure, high temperature gas which is expanded through a contoured convergent-divergent hypersonic nozzle after secondary diaphragm rupture.
In the scope of the present article HEG has been operated in a free-stream unit Reynolds number range between 1.4x10^6 /m and 9.8x10^6 /m at low total enthalpies around 3 MJ/kg. Typical test times for these conditions range between 2.5 and 3 ms.

3 Numerical methods

The NOLOT code, NOnLocal Transition analysis code Hein et al. (1994), was developed in cooperation with DLR and FOI and can be used for local as well as non-local analyses. The equations are derived from the conservation equations of mass, momentum and energy, which govern the flow of a viscous, compressible, ideal gas. All flow and material quantities are decomposed into a steady laminar base flow $\bar{q}$ and an unsteady disturbance flow $\tilde{q}$

$$q(x, y, z, t) = \bar{q}(x, y) + \tilde{q}(x, y, z, t). \tag{1}$$

The laminar base-flow $\bar{q}$ is calculated by the DLR FLOWer code Kroll and Fassbender (2005). The FLOWer code solves the compressible Navier Stokes equations for a perfect gas flow on block-structured grids, using second order finite volume techniques and cell-centered or cell vertex variables. The disturbance $\tilde{q}$ is represented as a harmonic wave

$$\tilde{q}(x, y, z, t) = \hat{q}(x, y) \exp[i(\alpha x + \beta z - \omega t)] \tag{2}$$

with the complex-valued amplitude function $\hat{q}$. In the following the hat over a variable denotes an amplitude function. In this paper the local approach is used, which is a subset of the nonlocal stability equations. Since NOLOT is a spatial code the wavenumbers α and β are complex quantities and the frequency ω is a real value. $-\alpha_i$ is the growth rate, which is the quantity of primary interest. The boundary conditions in NOLOT for a smooth wall (at $y = 0$) are:

$$\hat{u}_w,\ \hat{v}_w,\ \hat{w}_w,\ \hat{T}_w = 0. \tag{3}$$

The NOLOT code is validated by several test cases against published results, including DNS (direct numerical simulation), PSE (parabolized stability equations), multiple scales methods and LST (linear stability theory). A good summary of the validation is given by Hein et al. (1994). For the treatment of porous surfaces additional boundary conditions are implemented. The boundary conditions for porous walls are taken from Koslov et al. (2005) and Maslov (2003), a complete derivation can be found in these references. The conditions are given by

$$\hat{u}_w,\ \hat{v}_w,\ \hat{T}_w = 0, \quad \hat{w}_w = A\hat{p}_w, \tag{4}$$

where a subscript w denotes a value at the wall. The admittance A is the absorption coefficient and depends on the pore size, the flow quantities at the wall and at the upper boundary layer edge. A more detailed description is given by Wartemann et al. (2013). The verification of the in NOLOT implemented boundary conditions of porous walls against the Southampton LST code and direct numerical simulations is given in Wartemann et al. (2009) and Wartemann and Lüdeke (2010).

The boundary conditions used in the scope of the present study are based on equally spaced, blind, cylindrically pores. The pore size distribution of the here used C/C material with natural porosity was determined by means of mercury intrusion porosimetry. The porosity and the used hydraulic diameter, which are used for the calculations, is given in section 4.1.

For the calculation of the N-factors the most amplified wave angle is used and the frequency is kept constant

$$N = \ln \frac{a}{a_0} = \int_{s_0}^{s} -\alpha_i \, ds. \tag{5}$$

s_0 denotes the streamwise position where the disturbances starts to grow and a_0 is the amplitude at this position.

4 Experimental Setup

4.1 Model and Instrumentation

The model is a 7° half-angle blunted cone with an overall length of 1077 mm and an exchangeable nose tip. For the present experiments a nose radius of 2.5 mm radius was used. The model is equipped with a 835 mm long insert for the integration of an ultrasonically absorptive *carbon fibre reinforced carbon* (C/C) material. The insert starts at 182 mm from the model tip and covers 122° of the model surface in circumferential direction. Figure 2 shows the basic dimensions of the model. Special attention was payed to the model surface quality. To minimize potential discontinuities at junctions the model was machined with the C/C insert installed. The nose tip has been pre-machined separately and fitted to the main model by hand. The main model and the model tip were manufactured from stainless steel *(RAMAX2®)*.

The tested model was equipped with 49 flush mounted coaxial thermocouples of Typ E with a spacing of 33.3 mm to measure the transition location by means of surface heat flux evaluation. Thereof 25 transducers were installed along a line on the smooth model surface and 24 on the porous surface with the identical x-coordinate starting at 190 mm downstream the model tip.

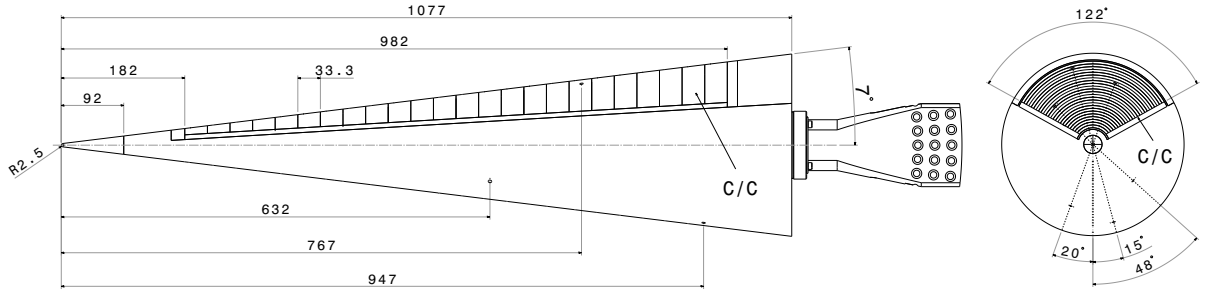

Figure 2: HEG wind tunnel model dimensions, based on a 2.5 mm nose radius.

Furthermore, in total 12 piezoelectric *PCB132A32* fast response pressure transducers were flush mounted along the model on the smooth and the porous surface at x = 632 mm, x = 767 mm and x = 947 mm measured from the nose tip. These pressure transducers cover a frequency range of 11 kHz to 1 MHz and were used to measure pressure fluctuations in the boundary-layer. Piezoelectric type pressure transducers are sensitive to accelerations. For this reason, the pressure transducers were installed using a silicone shroud to mechanically decouple the transducers and thus to reduce the transfer of high frequency vibrations from the model to the transducer. Blind reference pressure transducers of the same type without access to the flow field were used at each transducer location. The reference transducers were used to correct the readings for mechanical vibrations not associated with pressure fluctuations in the boundary layer. Additionally, 8 pressure transducers of type *KULITE XCL-100-100A* were installed to measure the surface pressure distribution along the model. The transducer positions on the model were chosen based on the experience gathered in previous transition studies on cone models in HEG, Wagner et al. (2011).
The model was supported by a sting system at its base at nominal zero angle of attack.

4.2 Ultrasonically Absorptive Material

About one third of the stainless steel surface was replaced by C/C, a fibre reinforced ceramic material. This material represents an intermediate state of the C/C-SiC manufacturing process Krenkel (2003) which is characterized by the following steps: By means of an autoclave technique, a green body of carbon fibre reinforced plastic (CFRP) is formed using commercially available 0|90° carbon fabrics impregnated with a phenolic resin. After curing, the green body is pyrolysed at temperatures of up to 1650 °C, which converts the phenolic matrix to amorphous carbon. This results in a C/C body containing random patterns of micro cracks. Carbon fibre reinforced carbon offers low expansion and specific weight as well as high temperature stability at protecting atmospheres. It can be reproduced very well and has already been tested widely for e.g. coated leading edges of hypersonic vehicles Glass et al. (2006); Glass (2008) and transpiration cooled combustion chamber applications Hald et al. (2009); Ortelt et al. (2010).

As depicted in figure 3, C/C material exhibits an orthotropic layout depending on the fabric layer orientation, which involves in-plane [1,2] and out-of-plane [3] (thermomechanical and flow-through) behavior. For the cone model, the ceramic insert was arranged such

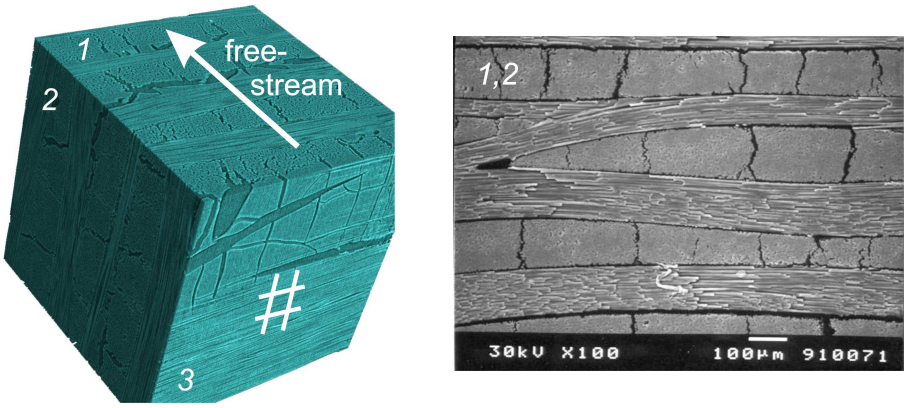

Figure 3: Computer tomography (left) and SEM picture (right) of C/C material.

that the fabric layers were oriented perpendicular to the free-stream direction. Figure 4 provides a close up image of the C/C material. The image shows that the dominant crack propagation direction is parallel to the fibre orientation and thus perpendicular to the free-stream. Furthermore, the infinite micro crack systems deeply penetrate the ceramic material and thus provide the potential to stabilize the acoustic modes in the boundary layer.

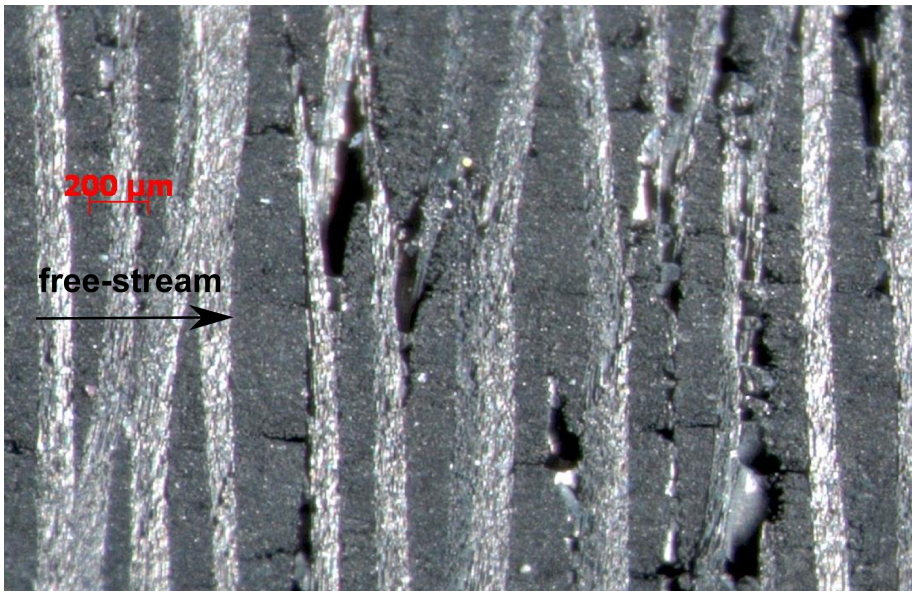

Figure 4: Carbon fibre reinforced carbon (C/C) on model insert after test campaign completion.

The model insert manufacturing involved the production of 24 C/C plates each with a thickness of 33.3 mm. By means of water jet cutting, the coarse contours were prepared. Each single ceramic part was glued onto an aluminum *(EN AW7075)* sub frame structure and additionally supplied by a guidance. The microstructure on the outer side of the porous material was not affected by the glue, which was investigated in the scope of a separate test. The assembled model was finished by means of ultrasonic milling to account for a high surface quality of the model surface. Finally, the porous material has

been cleaned in an ultrasonic bath to remove milling debris from the surface and the pores.
The C/C material used in the present study has an open porosity of 14.98 ± 0.25 %, a density of 1.3314 ± 0.0038 g/cm^3 and a minimum thickness of 5 mm which at the same time corresponds to the minimum pore depth.

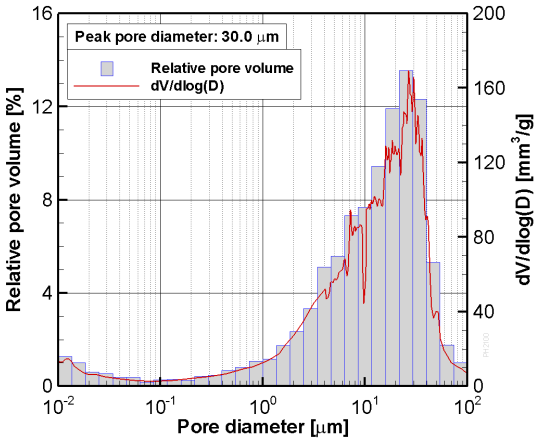

5.1: Sample 1

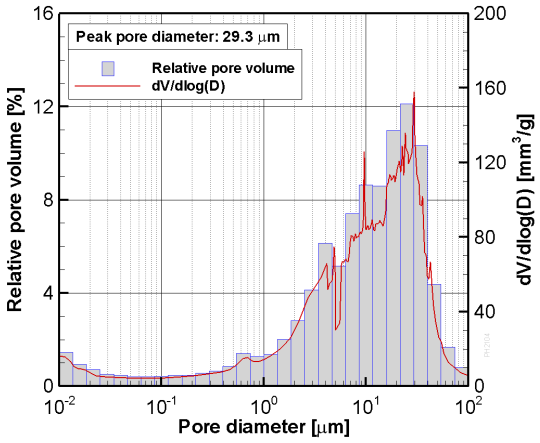

5.2: Sample 2

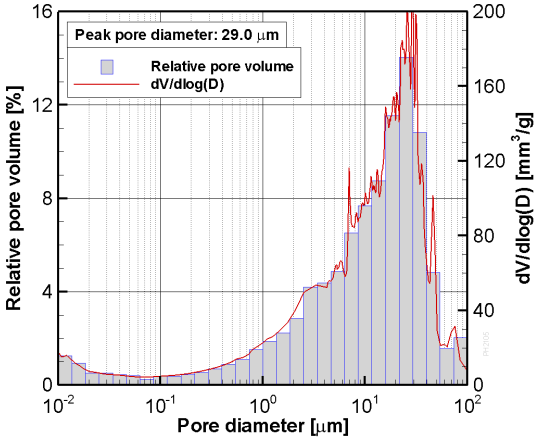

5.3: Sample 3

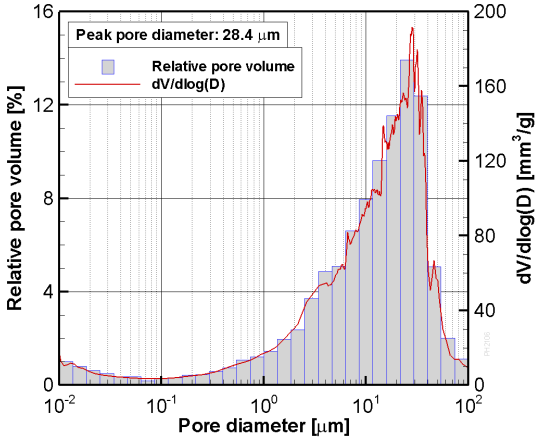

5.4: Sample 4

Figure 5: Pore size distributions for the applied C/C material.

The pore size distribution of the C/C material was determined by means of mercury intrusion porosimetry, where non-wetting mercury is intruded into the porous ceramic material. Based on applied external pressures of up to 200 MPa, the pore size distribution can be determined by detecting the infiltrated mercury volume and applying the Washburn equation. The pore size distribution has been determined for pore diameters between 0.01 µm and 100 µm, diameters beyond that range cannot be detected using this method. Figure 5 shows histograms of the relative pore volume for dedicated pore size ranges, which reflects the pore size distribution of the material. Furthermore, the corresponding gradient $dV/dlog(D)$ of displaced pore volumes normalized by the logarithm of the pore diameters is shown for four samples of the used material. This allows to determine the peak pore diameter, which is about 28 µm to 30 µm. All samples show a comparable and homogeneous distribution. It can be stated, that there is no single dominant pore

diameter, but rather a distinctive pore system for pore diameters between approximately 1 µm and 100 µm. Whereas smaller pore diameters might exist in regions at the fibre bundles itself, bigger pore diameters appear between the fabric layers, which is also visible in figure 4.

5 Results

5.1 Heat flux distribution

The above described model has been tested in HEG in a unit Reynolds number range of 1.4×10^6 /m to 6.4×10^6 /m for both radii. Additionally, a test at $\mathrm{Re_m} = 9.8 \times 10^6$ /m was conducted for the 2.5 mm nose radius to further investigate the Reynolds number dependency. In some cases the heat flux data, especially on the porous surface, were

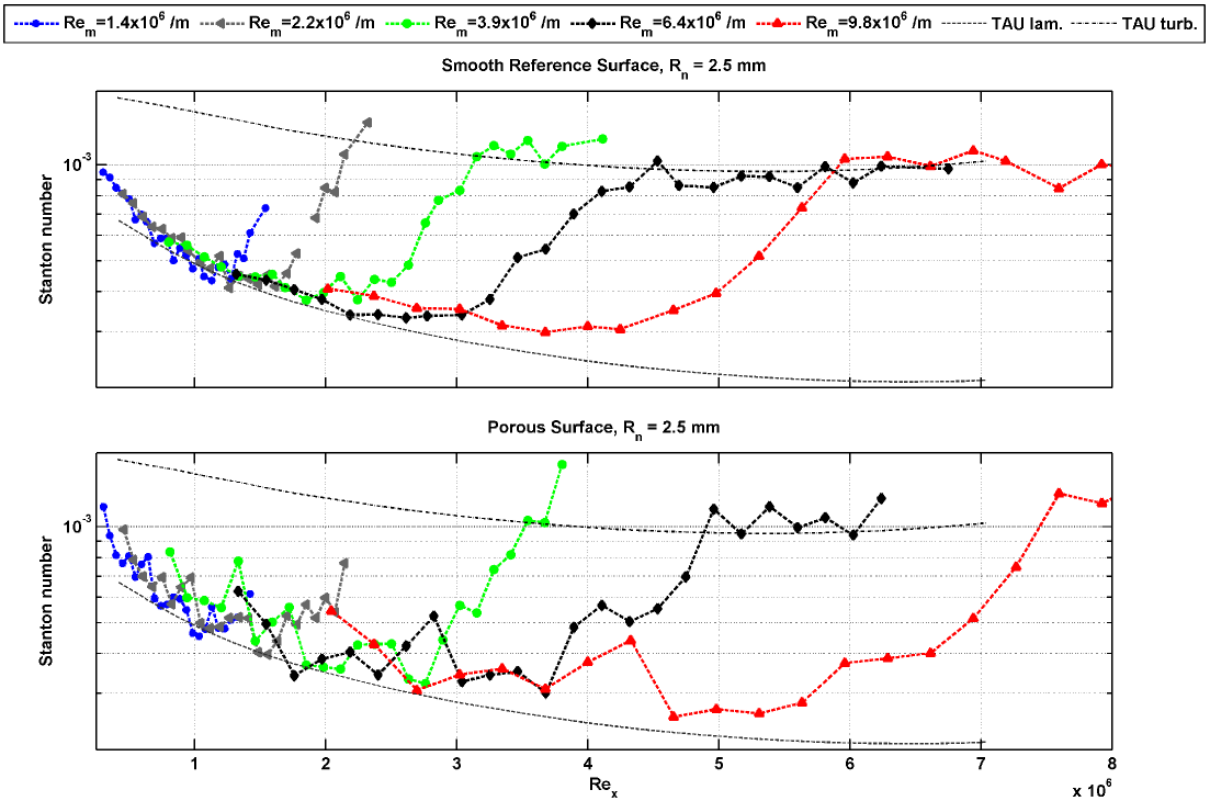

Figure 6: Heat flux distribution for various unit Reynolds numbers, $R_n = 2.5mm$.

subject to significant scatter close to the point of transition. It was found that defining the point of transition at the first distinct rise of heat flux towards the fully turbulent heat flux level provides the most repeatable results. Figure 6 provides the normalized heat flux distributions, in terms of Stanton number, on the smooth reference surface and the porous surface for $\mathrm{R_n} = 2.5$ mm. The figure shows a significant increase of the transition Reynolds number on the porous surface compared to the reference surface. Table 1 summarizes the transition Reynolds numbers on both sides of the model with respect to the unit Reynolds number. Relative transition Reynolds number increases between 0 % and 49 %

were observed whereas the damping efficiency of the porous surface seems to increas with unit Reynold number.

Figure 7 provides the normalized heat flux distribution for the tests with $R_n = 5$ mm. For a unit Reynolds number of $Re_m = 1.4 \times 10^6$ /m transition was not observed on cone model. First clear indications of transition on the porous surface were obtained for

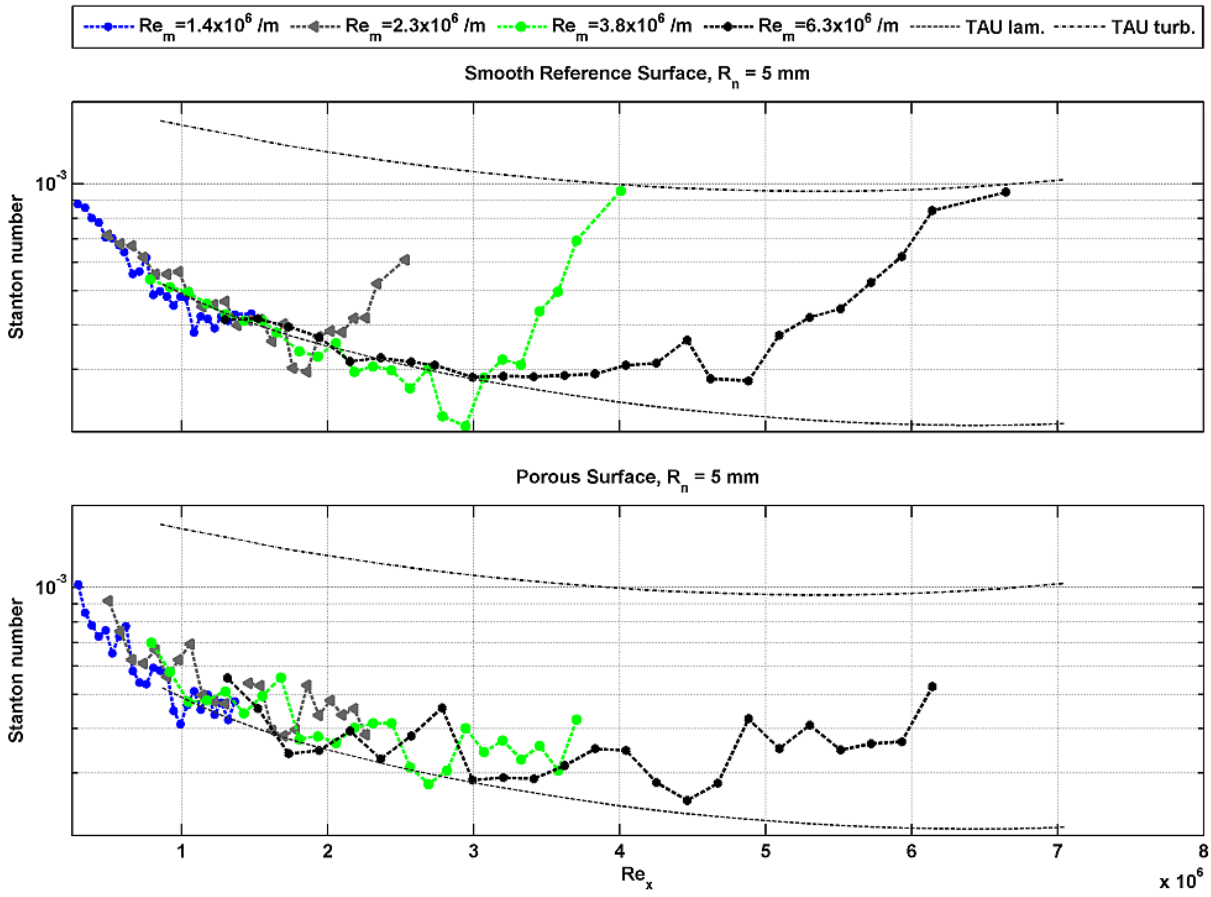

Figure 7: Heat flux distribution for various unit Reynolds numbers, $R_n = 5mm$.

$Re_m = 6.3 \times 10^6$ /m. Thus, the increase of the nose radius leads to a considerable delay of transition. Assuming a fully laminar boundary layer for $Re_m = 2.3 \times 10^6$ /m and $Re_m = 3.7 \times 10^6$ /m the increase of the transition Reynolds number corresponds to a minimum of 21 %.

Since the Reynolds numbers based on the nose radius, i.e. $Re_n = Re_m \times R_n$, is in

$Re_m[\times 10^6/m]$	$Re_{t,smooth}[\times 10^6]$	$Re_{t,porous}[\times 10^6]$	relative increase [%]
1.4	1.3	1.4	7
2.2	1.7	1.7	0
3.9	2.4	2.9	21
6.4	3.2	4.5	41
9.8	4.7	6.9	49

Table 1: Transition Reynolds numbers on smooth and porous surface, $R_n = 2.5$ mm.

the range of $Re_n = 3 \times 10^3$ to 3×10^4 the bluntness of the cone can be characterized as small. The observed increase of the transition Reynolds number with nose radius therefore follows the trend shown by Softley (1969).
The heat flux distributions on the smooth surface shown in figure 6 and figure 7 reveal a strong unit Reynolds number effect on the transition Reynolds number. To separate the delay of transition due to the unit Reynolds number effect from the transition delay caused by the ultrasonically absorptive C/C material figure 8 provides the transition Reynolds numbers as function of the free-stream unit Reynolds numbers.

All three data sets show a monotonic growth of $Re_t(Re_m)$ however, all with a different slope. For the smooth surface cases the slope represents the unit Reynolds number effect on the transition Reynolds number only. It can be seen that an increase of nose bluntness leads to a higher slope and thus to a stronger unit Reynolds number effect. In case of the porous surface the data set contains the effect of the unit Reynolds number and the effect of the porous material. Comparing the two data sets of the same bluntness a faster growth of Re_t with Re_m is found on the porous wall, this trend was first reported by Maslov et al. (2006) The difference between the two lines corresponds to the effect of the C/C material on the transition process and demonstrate the increase of the laminar run on the model surface.

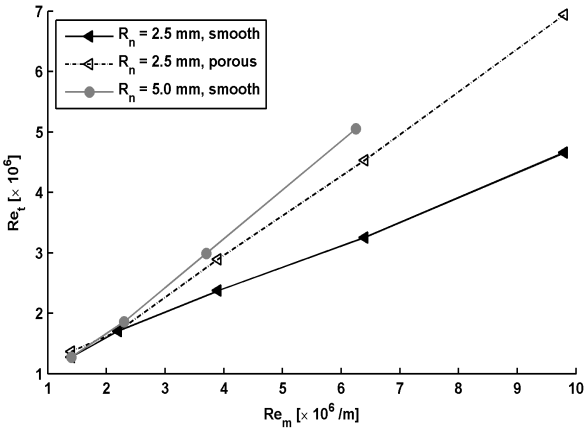

Figure 8: Transition Reynolds versus unit Reynolds number.

5.2 Second mode instabilities

The present section concentrates on the development of the second mode instabilities along the model on the smooth and the porous surface. Two test conditions have been chosen to investigate the instability growth along the model providing a laminar boundary layer of maximal length and a second mode instability strong enough to be detected, i.e. $Re_m = 1.4 \times 10^6$ /m for $R_n = 2.5$ mm and $Re_m = 2.3 \times 10^6$ /m for $R_n = 5$ mm. Figure 9 provides the amplitude density spectra of the pressure fluctuations measured in the boundary layer on both model sides at a unit Reynolds number of 1.4×10^6 /m and a nose radius of 2.5 mm. The data set was chosen out of six tests conducted with the same free-stream conditions. On the smooth surface the second mode can clearly be identified by the peak forming at around 250 kHz (x = 632 mm), 230 kHz (x = 767 mm) and 180 kHz (x = 947 mm). The second mode peaks show the characteristic shift towards lower frequencies in downstream direction due to the boundary layer thickening. The measured instability frequencies at the first two transducer locations are in good agreement with the NOLOT prediction in terms of peak frequency and instability growth. At the most downstream transducer location the boundary layer on the smooth surface be-

comes transitional (see figure 6) which leads to a broadening of the second mode peak and a stagnation of the amplitude growth compared to the NOLOT prediction. At the first

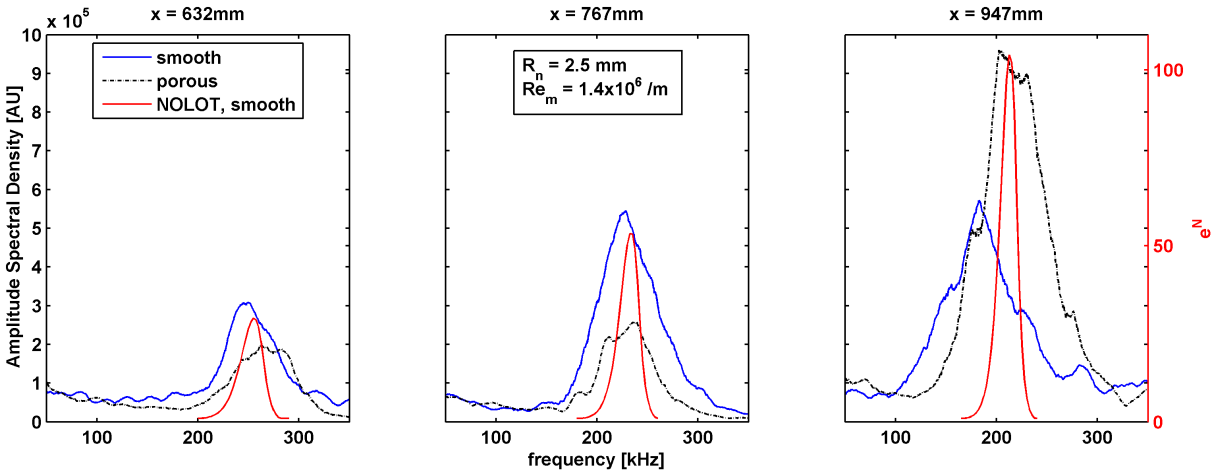

Figure 9: Second modes, NOLOT prediction for the smooth surface, $R_n = 2.5$ mm.

two transducer locations on the porous surface the second mode is measured with an amplitude corresponding to 64 % and 47 % of the smooth surface amplitudes. The observed reduction is a result of the damping mechanisms in the boundary layer above the porous surface. However, at the most downstream transducer location (x = 950 mm) the instability amplitude is increased by a factor of ≈ 3.7 compared to the value at x = 785 mm which is unexpectedly high.

At the same free-stream unit Reynolds number and a nose radius of $R_n = 5$ mm the

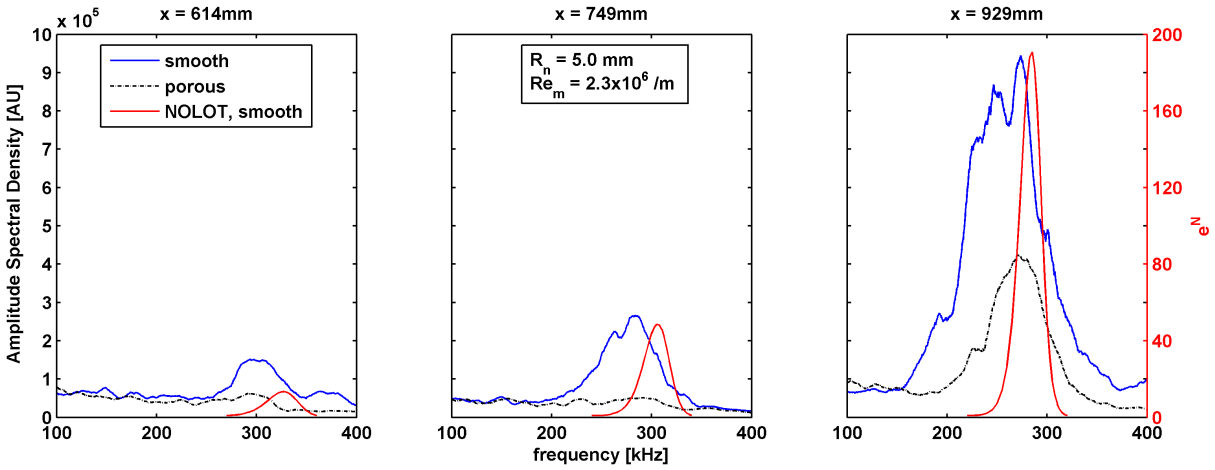

Figure 10: Second modes, NOLOT prediction for the smooth surface, $R_n = 5$ mm.

boundary layer remains fully laminar on both surfaces of the cone, see figure 7. No second mode instabilities could be detected in these cases. Therefore, the free-stream unit Reynolds number was increased to 2.3×10^6 /m. Figure 10 provides the corresponding amplitude density spectra of the pressure fluctuations in the boundary layer along the model. The second mode instabilities on the smooth surface are found to be in a frequency range of 300 kHz to 250 kHz. According to the heat flux distribution in figure 10

the most downstream transducer location is already in the transitional part of the boundary layer leading to an decrease of the second mode amplitude. The comparison with the NOLOT computation reveals an overprediction of the instability peak frequency and the growth rate. This overprediction might be caused by an uncertainty of the free-stream conditions. The amplitude density spectra corresponding to the first two transducers on the porous surface do not contain a significant peak above the noise floor which is a result of the ultrasonically absorptive surface. At the most downstream transducer location the second mode peak forms at $\approx$ 270 kHz with an amplitude significantly lower compared to the reference surface.

To resolve the second mode wave packages in the pressure fluctuations measured by the PCB transducers as a function of time a technique with a high time resolution is required. For that purpose, a continuous wavelet transform of the surface pressure traces using the Morlet wavelet was conducted, Bentley and McDonnell (1994). Figure 11b and 11c show the coefficients of the wavelet transforms for a frequency range between 100 kHz to 1 MHz on the smooth and the porous surface at x = 767 mm. A high coefficient represents

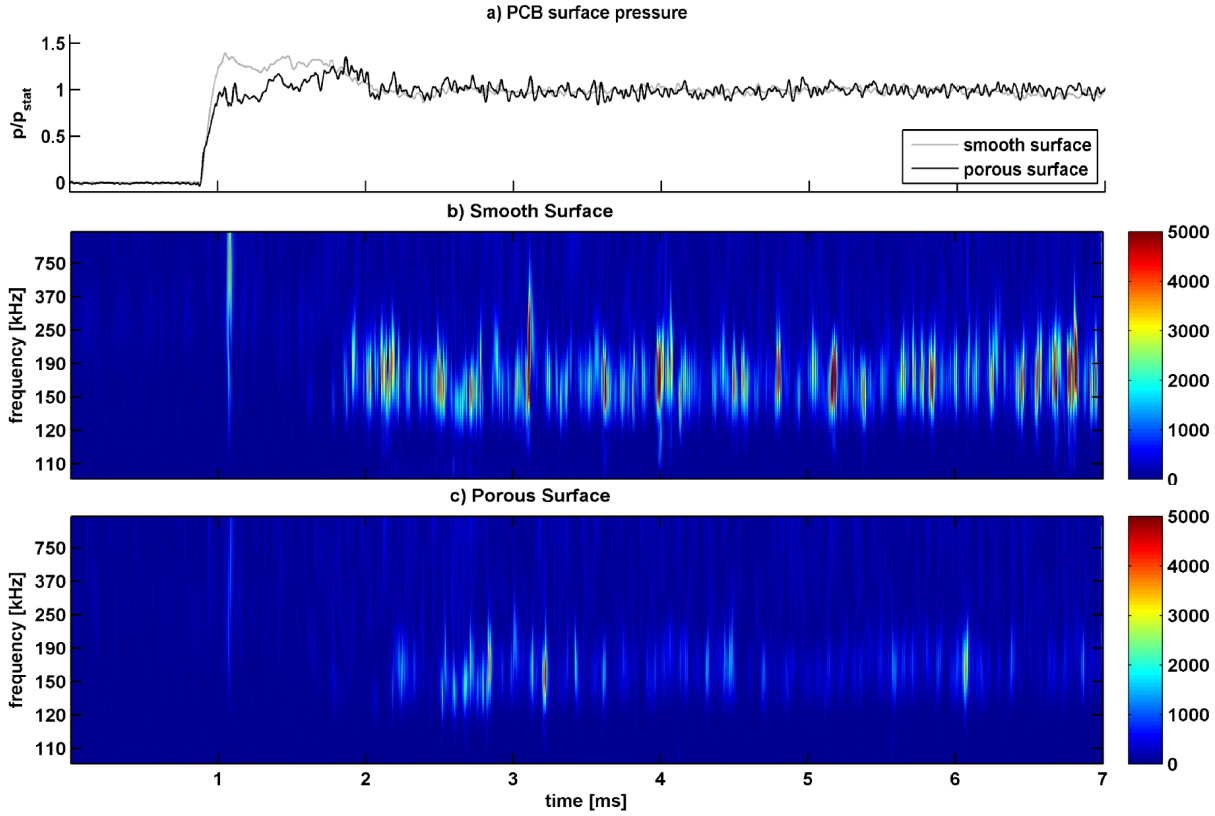

Figure 11: Wavelet analysis visualizing the presence of second mode waves during test time at x = 767 mm, $Re_m = 1.4 \times 10^6$ /m, $R_n = 2.5$ mm, a) surface pressure, b) smooth surface, c) porous surface.

a good correlation between the recorded surface pressure fluctuations and a Morlet type wavelet and thus stands in the present study for the presence of a second mode instability. Figure 11a shows the smoothed surface pressure traces of the evaluated transducers in the

time interval of 0 ms to 7 ms after shock reflection. The wavelet analysis reveals that the first second mode instabilities on the reference surface already appear about 1 ms after flow arrival. They remain present during the complete test time window which is defined between 3 ms and 6 ms. Furthermore, the instabilities are not continuously present in the the boundary layer. Instead, they are grouped in wave packages with different length in time. Finally, the comparison between the porous surface and the reference surface confirm the the C/C material being effective in damping the second instability.

6 Summary

The potential of an ultrasonically absorptive carbon-carbon material to delay hypersonic boundary layer transition has been investigated on a 7 degree half-angle blunted cone at zero angle of attack in the DLR High Enthalpy Shock Tunnel Göttingen (HEG) at Mach 7.5. The model was tested with nose radii of 2.5 mm and 5 mm. Heat flux and wall pressure fluctuation were measured on the porous carbon-carbon surface and a smooth reference surface at a unit Reynolds numbers range between 1.2×10^6 /m to 9.8×10^6 /m and 3 MJ/kg total enthalpy. It is shown that the porous surface significantly delays boundary layer transition by damping the second mode instabilities. The applied free-stream test conditions revealed a strong unit Reynolds number effect on the transition Reynolds number. Furthermore, it was found that damping efficiency of the C/C material increases with the free-stream unit Reynolds number and thus with the instability frequency.

To further the understanding of the observed 2nd mode damping above the porous surface more detailed studies including a characterization of the acoustic properties of the C/C material is required.

Acknowledgments

The presented work was conducted in the framework of the DLR project *IMENS-3C* and the FAST20XX project (Future High-Altitude High-Speed Transport 20XX). FAST20XX was coordinated by ESA-ESTEC and supported by the EU within the 7th Framework Program Theme7 Transport, Contract no.: ACP8-GA-2009-233816.
The support by Stuart Laurence and the HEG team during the test campaign is highly appreciated.

References

Bentley, P. and McDonnell, J. (1994). Wavelet transforms: an introduction. *Electronics & Communication Engineering Journal*.

Brès, G. A., Colonius, T., and Fedorov, A. V. (2010). Acoustic properties of porous coatings for hypersonic boundary-layer control. *AIAA Journal*, 48(2):267–274.

Fedorov, A., Kozlov, V., Shiplyuk, A., Maslov, A., and Malmuth, N. (2006). Stability of hypersonic boundary layer on porous wall with regular microstructure. *AIAA Journal*, 44(8):1866–1871.

Fedorov, A., Shiplyuk, A., Maslov, A., Burov, E., and Malmuth, N. (2003). Stabilization of a hypersonic boundary layer using an ultrasonically absorptive coating. *Journal of Fluid Mechanics*, 479:99–124.

Fedorov, A. V., Malmuth, N. D., Rasheed, A., and Hornung, H. G. (2001). Stabilization of hypersonic boundary layers by porous coatings. *AIAA*, 39(4):605–610.

Force, N. T. (1992). Report of the defense science board task force on the national aerospace plane (NASP). Technical report, Defense Science Board, Office of the Secretary of Defense , Washington, D.C. 20301-3140.

Glass, D., Dirling, R., Croop, H., Fry, T. J., and Frank, G. J. (2006). Materials development for hypersonic flight vehicles. In *14th AIAA/AHI Space Planes and Hypersonic Systems and Technologies Conference*, number AIAA 2006-8122, Canberra.

Glass, D. E. (2008). Ceramic matrix composite (CMC) thermal protection systems (TPS) and hot structures for hypersonic vehicles. In *15th AIAA Space Planes and Hypersonic Systems and Technologies Conference*, number AIAA 2008-2682, Dayton, OH.

Hald, H., Herbertz, A., Kuhn, M., and Ortelt, M. (2009). Technological aspects of transpiration cooled composite structures for thrust chamber applications. In *16th AIAA/DLR/DGLR International Space Planes and Hypersonic Systems and Technologies Conference*, number AIAA 2009-7222, Bremen.

Hannemann, K. and Martinez Schramm, J. (2007). *High Enthalpy, High Pressure Short Duration Testing of Hypersonic Flows, In: Springer Handbook of Experimental Fluid Mechanics*. Springer Berlin Heidelberg.

Hannemann, K., Martinez Schramm, J., and Karl, S. (2008). Recent extensions to the High Enthalpy Shock Tunnel Göttingen (HEG). In *Proceedings of the 2nd International ARA Days 'Ten Years after ARD'*, Arcachon, France.

Hein, S., Bertolotti, F. P., Simen, M., Hanifi, A., and Henningson, D. (1994). Linear nonlocal instability analysis - the linear nolot code. Technical Report IB-223-94 A56, DLR.

Koslov, V. F., Fedorov, A. V., and Malmuth, N. D. (2005). Acoustic properties of rarefied gases inside pores of simple geometries. *Journal of the Acoustical Society of America*, 117 (6):pp. 3402–3412.

Krenkel, W. (2003). Applications of fibre reinforced C/C-SiC ceramics. *Ceramic Forum International*, 80(8):31–38.

Kroll, N. and Fassbender, J. K. (2005). *MEGAFLOW - Numerical Flow Simulation for Aircraft Design*. Springer Berlin.

Laurence, S., Wagner, A., Hannemann, K., Wartemann, V., Lüdeke, H., Tanno, H., and Ito, K. (2012). Time-resolved visualization of instability waves in a hypersonic boundary layer. *AIAA Journal*, Vol. 50(1):243–246.

Lukashevich, S. V., Maslov, A. A., Shiplyuk, A. N., Fedorov, A. V., and Soudakov, V. G. (2012). Stabilization of high-speed boundary layer using porous coatings of various thicknesses. *AIAA Journal*, 50(9):1897–1904.

Malik, M. R. (1989). Prediction and control of transition in supersonic and hypersonic boundary layers. *AIAA Journal*, 27(11):1487–1493.

Malmuth, N., Fedorov, A., Shalaev, V., Cole, J., Khokhlov, A., Hites, M., and Williams, D. (1998). Problems in high speed flow prediction relevant to control. Number AIAA 98-2695.

Maslov, A. (2003). Experimental and theoretical studies of hypersonic laminar flow control using ultrasonically absorptive coatings (uac). Technical report, ISTC 2172-2001.

Maslov, A., Shiplyuk, A., Sidorenko, A., Polivanov, P., Fedorov, A., Kozlov, V., and Malmuth, N. (2006). Hypersonic laminar flow control using a porous coating of random microstructure. In *44th AIAA Aerospace Sciences Meeting and Exhibit*, Reno, Nevada. AIAA 2006-1112.

Maslov, A. A., Fedorov, A. V., Bountin, D. A., Shiplyuk, A. N., Sidorenko, A. A., Malmuth, N., and Knauss, H. (2008). Experimental study of transition in hypersonic boundary layer on ultrasonically absorptive coating with random porosity. In *46th AIAA Aerospace Sciences Meeting and Exhibit*, number 2008-587, Reno, Nevada. AIAA.

Ortelt, M., Herbertz, A., and Hald, H. (2010). Investigations on fibre reinforced combustion chamber structures under effusion cooled LOX/LH2 operation. In *45th AIAA/ASME/SAE/ASEE Joint Propulsion Conference & Exhibit*, number AIAA 2009-5475, Denver, CO.

Rasheed, A., Hornung, H. G., Fedorov, A. V., and Malmuth, N. D. (2002). Experiments on passive hypervelocity boundary-layer control using an ultrasonically absorptive surface. *AIAA*, 40(3):481–489.

Softley, E. J. (1969). Boundary layer transition on hypersonic blunt, slender cones. In *AIAA Paper*, number AIAA69-705.

Turner, J., Hörschgen, M., Jung, W., Stamminger, A., and Turner, P. (2006). SHEFEX Hypersonic re-entry flight experiment; vehicle and subsystem design, flight performance and prospects. In *14th AIAA/AHI Space Planes and Hypersonic Systems and Technologies Conference*, number AIAA 2006-8115.

Wagner, A., Hannemann, K., Wartemann, V., Tanno, H., and Katsuhiro, I. (2012). Free piston driven shock tunnel hypersonic boundary layer transition experiments on a cone configuration. In *AVT - Specialists' Meeting on Hypersonic Laminar-Turbulent Transition*, RTO-MP-AVT-200, San Diego, California, USA. RTO.

Wagner, A., Laurence, S., Martinez Schramm, J., Hannemann, K., Wartemann, V., Lüdeke, H., Tanno, H., and Ito, K. (2011). Experimental investigation of hypersonic boundary-layer transition on a cone model in the High Enthalpy Shock Tunnel Göttigen (HEG) at Mach 7.5. In *17th AIAA International Space Planes and Hypersonic Systems and Technologies Conference*, number AIAA 2011-2374, San Francisco, California, USA.

Wartemann, V., Giese, T., Eggers, T., Wagner, A., and Hannemann, K. (2013). Hypersonic boundary-layer stabilization by means of ultrasonically absorptive carbon-carbon material - part 2: Computational analysis. In *51st AIAA Aerospace Sciences Meeting*, Texas.

Wartemann, V. and Lüdeke, H. (2010). Investigation of slip boundary conditions of hypersonic flow over microporous surfaces. In *V European Conference on Computational Fluid Dynamics*, Lisbon, Portugal. ECCOMAS CFD.

Wartemann, V., Lüdeke, H., and Sandham, N. (2009). Stability analysis of hypersonic boundary layer flow over microporous surfaces. In *16th AIAA/DLR/DGLR International Space Planes and Hypersonic Systems and Technologies Conference*, number AIAA 2009 - 7207, Bremen, Germany.

Wartemann, V., Lüdeke, H., and Sandham, N. D. (2012a). Numerical investigation of hypersonic boundary-layer stabilization by porous surfaces. *AIAA Journal*, 50(6):1281–1290.

Wartemann, V., Willems, S., and Gülhan, A. (2012b). Mack mode damping by micropores on a cone in hypersonic flow. In *AVT-200, Hypersonic Laminar-Turbulent Transition*, San Diego.

Weihs, H., Longo, J., and Turner, J. (2008). Key experiments within the SHEFEX II mission. In *IAC 2008*, number IAC-08.D2.6.4, Glasgow, Scottland UK.